Biosensors and Bioelectronics 156 (2020) 112145

Contents lists available at ScienceDirect

Biosensors and Bioelectronics

journal homepage: http://www.elsevier.com/locate/bios

In situ fabrication of aloe-like Au–ZnO micro/nanoarrays for ultrasensitive biosensing of catechol

Tao Liu, Qiang Zhao, Ying Xie, Danfeng Jiang, Zhenyu Chu *, Wanqin Jin **

State Key Laboratory of Materials-Oriented Chemical Engineering, College of Chemical Engineering, Nanjing Tech University, Nanjing, 210009, PR China

ARTICLE INFO

Keywords:
Catechol biosensor
Aloe-like composite
Au–ZnO micro/Nanoarrays
Real water detection

ABSTRACT

Currently, the large-scale and controllable fabrication of nanostructures on substrates remains a great challenge for further practical applications. In this work, a novel 3D aloe-like Au–ZnO nanocomposite was designed for *in situ* synthesis on an ITO substrate, achieving real-time detection of trace catechol (CC) in water. A seed-assisted hydrothermal approach was proposed to control the crystal distribution and growth direction to build a ZnO aloe-like architecture. To eliminate the natural weak conductivity of ZnO, Au nanoparticles were further deposited on all ZnO arrays to construct Au–ZnO micro/nanostructures. The synergetic effects derived from the aloe-like ZnO with a large specific area and Au nanoparticles with high conductivity resulted in both high electrocatalysis and fast electron transfer in enzymatic reactions. After laccase immobilization, the as-prepared biosensor exhibited specific recognition of catechol among other dihydroxybenzenes and phenol with an ultrahigh sensitivity of 131 μA mM^{-1}, as well as an extremely wide linear range from 75 nM to 1100 μM and an ultralow detection limit of 25 nM. In addition, in the detection of real lake samples, this biosensor showed satisfactory anti-interference ability and provided reliable assay results.

1. Introduction

Phenolic compounds, which are hypertoxic and non-degradable pollutants, have caused severe damage to the environment and human health in the last decade (Abbas et al., 2019). With the rapid societal and economic development, phenolic substances are being widely discharged into water and soil due to various human industrial activities (Bensalah et al., 2005; Liu et al., 2019). According to the integrated wastewater discharge standard of China, the maximum permitted concentration of phenolic substances is 0.4 mg/L. Catechol (CC) is a typical phenolic compound that is listed as a potential human carcinogen even at a low concentration (Ameer and Adeloju, 2009; Wang et al., 2007). Therefore, its fast and *in situ* monitoring in industrial regions is essential to providing early warning of sudden leaks to prevent further pollutant diffusion. However, traditional CC analysis techniques, such as high-performance liquid chromatography (HPLC) (Jiao et al., 2018) and gas chromatography/mass spectrometry (GC/MS) (Moldoveanu and Kiser, 2007), are rarely used for immediate and on-site reports of pollutant concentrations due to their long detection period, complicated pre-treatment operation and large instrument requirements (Cardoso et al., 2019).

Compared with other analysis methods, electrochemical biosensors are advanced in terms of their fast response, portable size and real-time detection mode, arousing wide attention in the fields of environmental monitoring, the food industry, fermentation processes and clinical medicine (Bansod et al., 2017; Jiang et al., 2016; Samphao et al., 2018; Sani et al., 2018). For CC detection, laccase often serves as the bio-recognizer; its redox ability, derived from the copper in the flavin adenine dinucleotide (FAD) (Palanisamy et al., 2017; Jiang et al., 2019), enables the following reaction:

$$\text{Catechol} \xrightarrow{laccase} \text{o} - \text{benzoquinone} + 2H^+ + 2e^- \quad (1)$$

Normally, in polluted lakes or seas, CC coexists with many other phenolic compounds with low oxidation potentials. Hence, accurate determination of CC is subject to great interference from the extra electro-oxidation of other compounds. However, biosensing sensitivity is strongly dependent on the potential. A higher overpotential often produces higher performance but low selectivity (Chu et al., 2017; Hu et al., 2020). In this case, enhancing the electrocatalysis of the electrode material under a low potential is desired to satisfy the needs of practical

* Corresponding author.
** Corresponding author.
E-mail addresses: zychu@njtech.edu.cn (Z. Chu), wqjin@njtech.edu.cn (W. Jin).

https://doi.org/10.1016/j.bios.2020.112145
Received 16 January 2020; Received in revised form 25 February 2020; Accepted 8 March 2020
Available online 16 March 2020

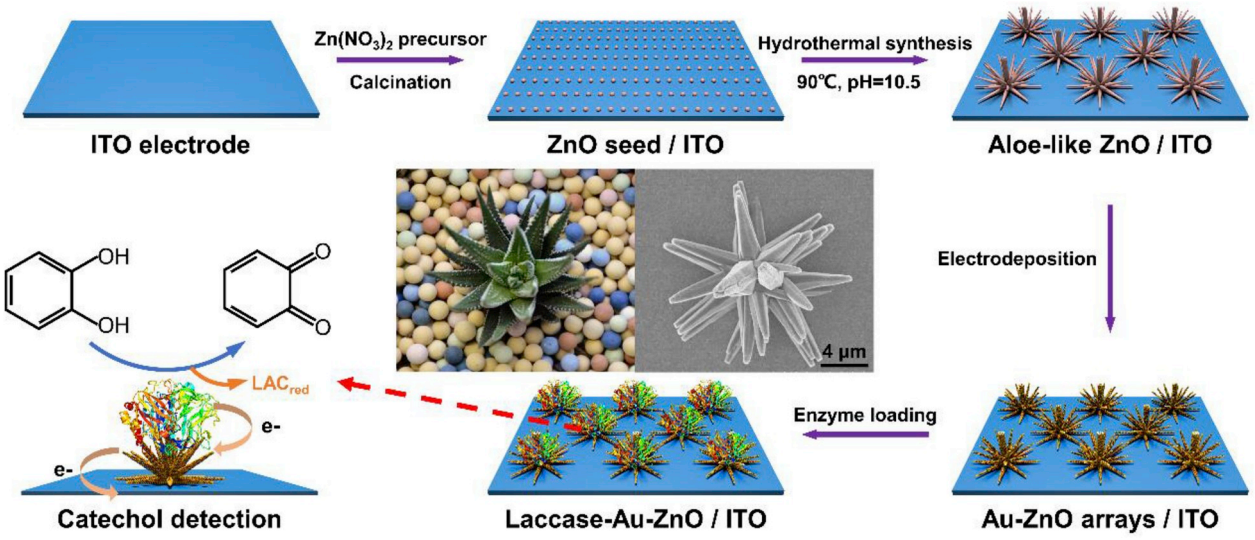

Fig. 1. Schematic illustration of the preparation of aloe-like Au–ZnO arrays on an ITO electrode.

applications.

Nanostructured zinc oxide (ZnO), a well-known semiconductor material, plays a critical role in optics, optoelectronics and sensors due to its excellent catalysis, high specific surface area, good biocompatibility and non-toxicity (Shetti et al., 2019; Yue et al., 2019). In addition, enzymes can easily adsorb on the ZnO surface owing to its high isoelectric point (IEP) of approximately 9.5 (Shetti et al., 2019), showing the potential to promote enzymatic reactions. Among various nanostructures, the aloe-like shape of ZnO nanocrystals shows an extremely large 3D surface that is able to provide more catalytic sites than other materials for electrochemical oxidation. Nevertheless, in the electrochemical biosensing process, its deficiency of poor conductivity will strongly block electron transfer, reducing performance (Wang et al., 2019; Usha and Gupta, 2018). Meanwhile, the high activation potential of ZnO nanocrystals for the redox of zinc can easily cause interference, affecting the detection accuracy (Zhao et al., 2013).

To overcome the above obstacles, we here proposed an ultrasensitive and accurate catechol biosensor constructed from Au nanoparticle-decorated aloe-like ZnO arrays. As shown in Fig. 1, anisotropic ZnO nanorods derived from ZnO seeds were simultaneously grown to assemble an aloe-like shape. Abundant AuNPs with a size of 90 nm were then electrodeposited to decorate the ZnO surface to strongly enhance the conductivity. The synergistic effects from the high catalytic area of the aloe-like architecture and the fast electron transfer ability of the AuNPs obviously magnify the current response signal during the electrochemical process. This nanocomposite promotes the adsorption of laccase for the fabrication of a catechol biosensor and shows specific recognition of catechol at a very low working potential with outstanding sensitivity and accuracy in real lake samples.

2. Experiments

2.1. Reagents and apparatus

ITO electrodes (10 mm × 20 mm × 1.1 mm, resistance ≤ 7 Ω) were purchased from South China Science & Technology Company. Potassium ferricyanide ($K_3Fe(CN)_6$), laccase (EC 1.10.3.2, 285.7 unit/mg, from Rhus vernicifera) and trizma base ($C_4H_{11}NO_3$, ≥99.9%) were obtained from Sigma-Aldrich. Zinc nitrate hexahydrate ($Zn(NO_3)_2{\cdot}6H_2O$, 99%) and hexamethylenetetramine (HMTA, 99.5%) were obtained from Aladdin, China. Chloroauric acid ($HAuCl_4$, ≥99%), phenol (PE), catechol (CC), resorcine (RC), hydroquinone (HQ), uric acid (UA), ascorbic acid (AA) and glutaraldehyde (25% aqueous solution) were provided by Sinopharm Chemical Reagent Co., Ltd., China. Ammonia ($NH_3{\cdot}H_2O$, 25 wt%), acetone (C_3H_6O, 99.5%), KCl, KH_2PO_4 and K_2HPO_4 were supplied by Shanghai Lingfeng Chemical Reagent Co., Ltd., China. All the chemicals in this work were directly used without further purification. All aqueous solutions were prepared with deionized water (≥18.2 MΩ, Smart2Pure 6, Thermo Fisher Scientific, USA).

A field emission scanning electron microscope (FESEM, Hitachi, S-4800) was used to observe the surface morphology of the synthesized electrode interface. An X-ray diffractometer (D/MAX 2500 V/PC) with Cu-Ka radiation (0.15419 nm) was employed to measure the characteristic peaks of ITO, ZnO and Au–ZnO. An X-ray photoelectron spectrometer (XPS, ESCALAB MKLL) was utilized to analyse the elemental valence states of Au and Zn.

2.2. Preparation of aloe-like ZnO array-modified ITO electrode

ZnO/ITO was prepared through a modified wet chemical process (Greene et al., 2005; Lee et al., 2011). First, an ITO electrode was ultrasonically cleaned in acetone, ethanol and deionized water for 15 min each. Then, a ZnO seed layer was formed on the ITO electrode via a spin-coating method with 60 μL of $Zn(NO_3)_2$/ethanol solution (0.01 M) and sintered at 350 °C for 30 min in air atmosphere.

$Zn(NO_3)_2$ (0.02 M) and HMTA (0.02 M) were used to prepare the precursor solution, and ammonia was added to adjust the pH value to alkaline. The ZnO seed/ITO was immersed into the precursor solution at 90 °C for 2 h. After the hydrothermal reaction, the electrode was rinsed with deionized water and ethanol 3 times.

2.3. Synthesis of Au–ZnO modified electrode

Au–ZnO/ITO was prepared through an electrodeposition method. $HAuCl_4$ was prepared as the electrolyte (2 mM), and trizma base was dissolved to adjust the pH value to 7.0. After the hydrothermal process, the surface of the aloe-like ZnO was coated with adsorbed Zn^{2+}. Due to electrostatic force, $AuCl_4^-$ could easily accumulate on the surface of the ZnO. In the electrodeposition process, the above ZnO-modified ITO electrode served as the working electrode, and chronoamperometry was adopted with a potential of −0.2 V and deposition time of 150 s. After that, the obtained electrode was rinsed with deionized water and dried at 50 °C.

2.4. Immobilization of laccase

Laccase (100 U) was dissolved in 1 mL of phosphate buffer solution

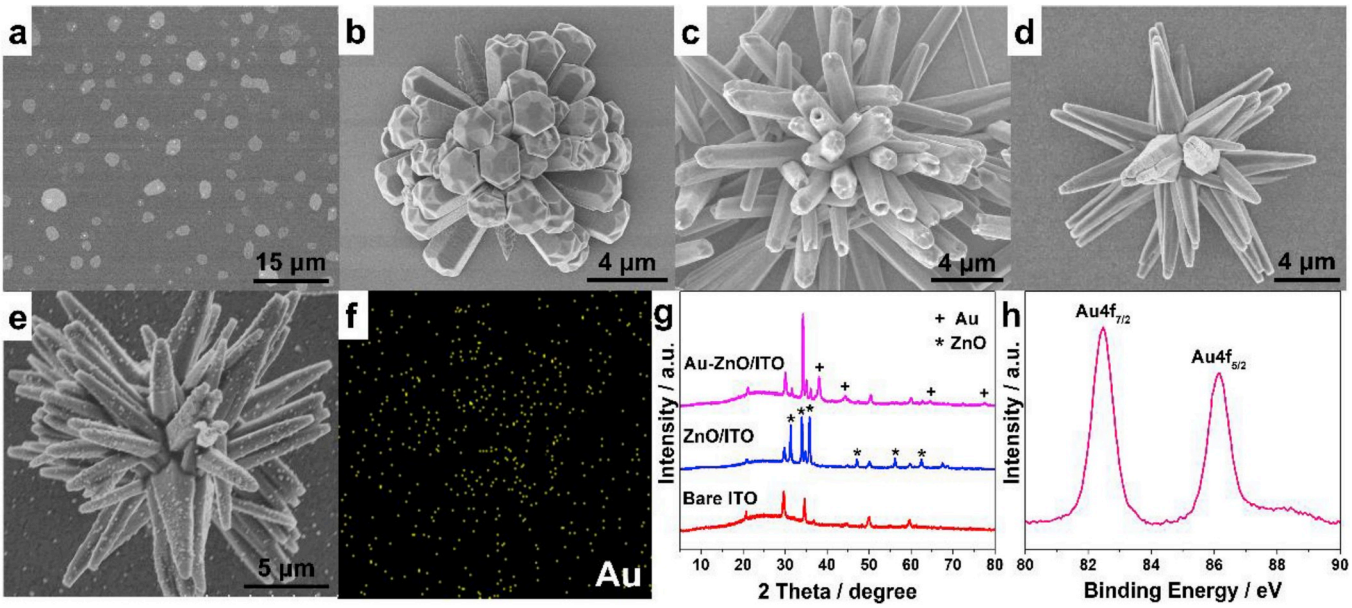

Fig. 2. FESEM images of (a) a seed layer synthetized by the spin-coating method, (b–d) aloe-like ZnO synthesized at different pH values (b: pH = 6.5, c: pH = 8.5, d: pH = 10.5), and (e) a single Au–ZnO nanocrystal obtained with an electrodeposition time of 150 s; (f) EDX mapping results for Au; (g) XRD patterns of bare ITO, ZnO/ITO and Au–ZnO/ITO; (h) XPS spectrum of Au4f.

(PBS, 0.1 M, pH = 7.0), and then 12.5 μL of glutaraldehyde was added to crosslink the enzyme. After that, 100 μL of enzyme solution was dropped on the as-prepared Au–ZnO/ITO electrode.

2.5. Electrochemical measurements

All electrochemical experiments, including cyclic voltammetry (CV), electrochemical impedance spectroscopy (EIS) and chronoamperometry, were performed with a CHI660E electrochemical workstation (Shanghai Chenhua Instrument Co., Ltd., China). In addition, 10 mM of phosphate buffer solution (PBS, pH = 6.5) containing 0.1 M of KCl was used for all the electrochemical tests. A conventional three-electrode configuration was employed during the experiment. The modified ITO electrode, a Pt wire and an Ag/AgCl (saturated KCl) electrode were utilized as the working electrode, counter electrode and reference electrode, respectively.

3. Results and discussion

3.1. Nanostructure evolution of the aloe-like Au–ZnO arrays

In our design, a secondary growth process after seeding was required to build the aloe-like morphology of the ZnO arrays to achieve a large specific area. We sought to control the distribution of ZnO crystals on the ITO substrate to avoid obvious aggregation by modifying the seed density. If a seed layer is not provided, as shown in Fig. S1a, the weak binding force between ZnO and the ITO surface restricts nucleation growth on the electrode, leading to the formation of few irregular ZnO crystals on the bare ITO electrode. In this case, we tried two different seeding methods (spin-coating and dip-coating) to investigate the influence of seeds (Fig. S1). Only by using the spin-coating route did the seed feature observed in Fig. 2a, showing a very uniform distribution of tiny crystals. Then, further growth produced a homogenous arrangement of ZnO arrays (Fig. S1b). In addition, the optimum deposition number of seed layers was studied as shown in Figs. S2a–S2c. A single layer produced many large blank areas without seeds, while overcrowded crystals were obtained if the seed coating was increased to 3 layers. Two layers of seed deposition are appropriate to restrain crystal stacking and enable the further growth of aloe-like ZnO arrays (Fig. S2b).

Due to instability in an acidic environment, the nanostructure of ZnO is sensitive to the pH value during the synthesis process (Shahamirifard and Ghaedi, 2019; Ying et al., 2019). Therefore, in this hydrothermal growth approach, the influence of pH values from 6.5 to 10.5 on the crystal morphology was investigated through the addition of ammonia (Fig. 2b–d) since ZnO cannot crystallize below a pH of 6.5. Moreover, to create anisotropic crystal formation, HMTA, a nonpolar chelating agent, was employed as an inducer. During the reaction, HMTA can adsorb on the nonpolar crystal plane of ZnO crystals to control the orientation of crystal growth (Parize et al., 2016). As shown in Fig. 2b, although a series of ZnO nanorods pointing in various orientations were formed in neutral solution, the heavy accumulation behaviour among the crystal rods weakened the advantage of the high surface area. The results were quite different when the pH value was raised to a weakly alkaline value (Fig. 2c). Too many rods were created with random intergrowth as well as large differences in rod length, diameter and shape. Upon increasing the pH value to 10.5, a clear and aloe-like structure was obtained through the uniform assembly of nanorods with a diameter of ca. 150 nm and a length of 6 μm. Moreover, these micro/nanoflowers were independent with rare aggregation, and a certain distance was maintained between them (Fig. 2d), which is beneficial to superior electrocatalysis because of the formation of numerous sensing units. However, if the pH value was further increased to 11.0, almost all Zn was transformed to Zn $(NH_3)_4^{2+}$ (Fujii et al., 2017); hence, ZnO crystals were rarely observed on the substrate.

The growth mechanism of the aloe-like structure was studied under the above optimized conditions (Fig. S3). After 40 min of hydrothermal synthesis, the complete aloe-like morphology first appeared with sharp ZnO terminals and an uneven surface (Fig. S3c). In the following synthesis process, the terminals tended to form hexagonal shapes, and a smooth surface was obtained after 80 min of growth (Figs. S3d and S3e). The XRD pattern showed that the anisotropic growth of aloe-like ZnO gives priority to the (002) crystal plane (Fig. S3f).

To promote the conductivity of the ZnO material, gold nanoparticles were then electrodeposited onto the ZnO surface. Within 100 s, few AuNPs were obtained on the surfaces of the ZnO nanorods, indicating insufficient synthesis (Fig. S4a). Upon reaching 150 s, AuNPs were uniformly distributed over the entire ZnO surface with an average size of

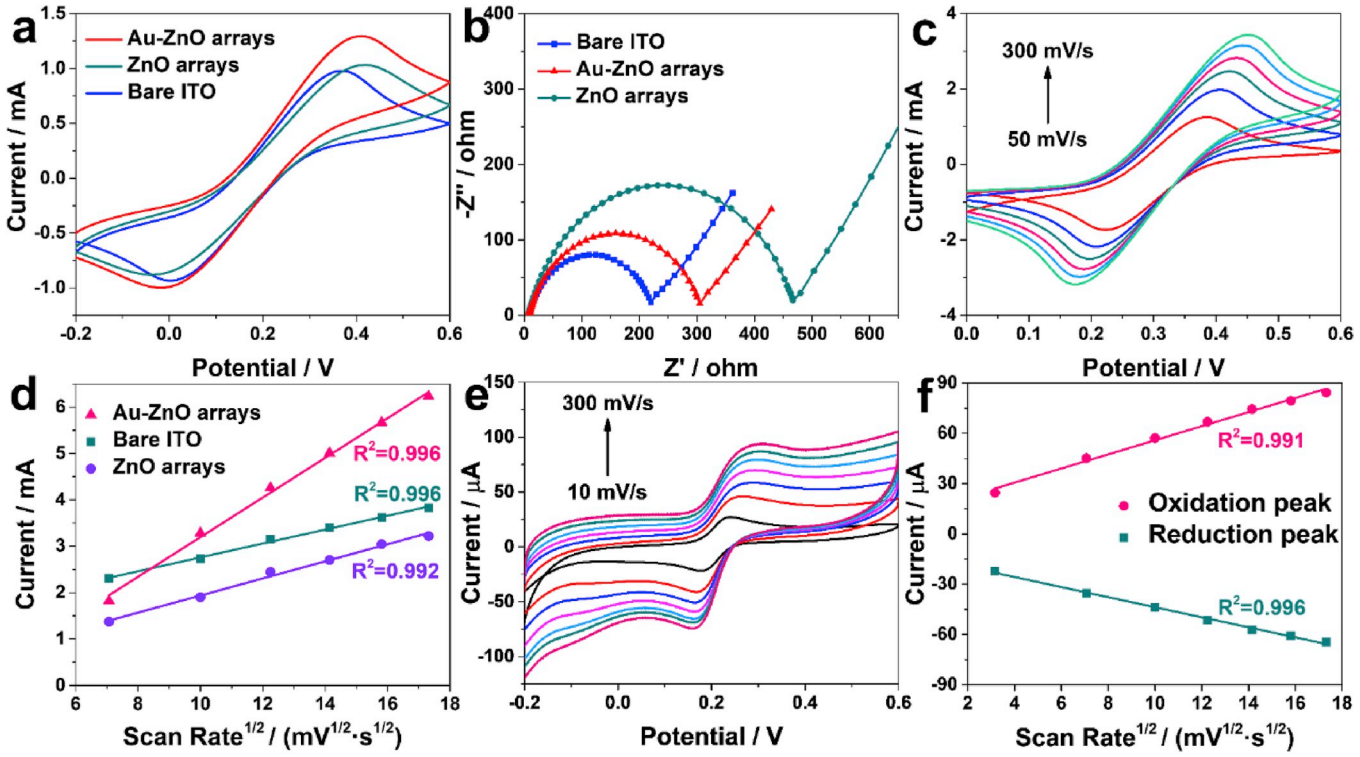

Fig. 3. (a) CV behaviours of bare, ZnO-modified, and Au–ZnO-modified ITO electrodes in the presence of 10 mM of $[Fe(CN)_6]^{3-/4-}$ containing 0.1 M of KCl with a scanning rate of 50 mV/s; (b) Nyquist plots of different electrodes in the presence of 5 mM of $[Fe(CN)_6]^{3-/4-}$ solution containing 0.1 M of KCl; (c) CV curves of Au–ZnO/ITO electrodes in a system containing 10 mM of $K_3Fe(CN)_6$ and 3 M of KCl at different scanning rates from 50 to 300 mV/s; (d) calibration curves for the peak current vs. the square root of scan rate for bare, ZnO-modified, and Au–ZnO-modified ITO electrodes. (e) CV curves of the as-prepared biosensor at different scanning rates in PBS containing 75 μM of CC. (f) calibration curves for the peak current vs. the square root of scan rate.

90 nm (Figs. 2e and S6). However, further deposition only produced over-aggregation, generating many larger particles with irregular features (Fig. S4b). Furthermore, the EDX results (Fig. 2f) indicate that gold was mainly distributed on the nanorods of the aloe-like crystals. This result occurred because the surface of ZnO often possesses abundant Zn^{2+} after hydrothermal reaction, which can easily adsorb $AuCl_{4-}$ through the electrostatic force (Jiang et al., 2018; You et al., 2019).

Three samples of bare ITO, ZnO/ITO and Au–ZnO/ITO were scanned by XRD to clarify the crystallization behaviours of each material (Fig. 2g). In the results for bare ITO, the characteristic peaks located at 31.8°, 34.4°, 36.2°, 47.5°, 56.5° and 62.8° represented the ZnO crystal planes of (100), (002), (101), (102), (110) and (103), respectively, which were in good agreement with those of the zincite phase of ZnO (JCPDS 036–1451) (García-Farrera and Velásquez-García, 2019). Once AuNPs had been deposited on the ZnO crystal, two peaks at 37.9° and 44.8°, which indicated the (111) and (200) planes of Au, were observed, confirming the formation of the nanocomposite (Cho et al., 2019; Shi et al., 2017). Then, this nanocomposite was analysed by XPS to confirm its chemical composition before and after Au deposition. According to the comparison of the full survey spectra in Fig. S5a, the Au peak appeared after the electrodeposition process, and other peaks were almost unchanged, including the Zn2p peaks (Fig. S5b) (Chang et al., 2019). This result indicates that the introduction of AuNPs cannot produce obvious chemical bonding to ZnO crystals. In addition, details in the Au spectra (Fig. 2h) show that there are two peaks located at 82.6 eV and 86.2 eV, which coincide with the core-level emissions of $Au4f^{7/2}$ and $Au4f^{5/2}$, respectively (Kim et al., 2015). This result demonstrated that the adsorbed AuNPs on the ZnO surface were classified as elemental Au.

3.2. Electrochemical behaviours of the Au–ZnO-based electrodes

The electrochemical redox ability of the as-prepared nanocomposite, which is determined by the electrocatalytic activity and conductivity, was evaluated through its CV performance. Compared to the bare ITO electrode, the introduction of ZnO minimally intensified the current signal, only peak potential difference (ΔEp) increased, indicating an increase in electron transfer resistance (Fig. 3a). This effect is attributed to the poor conductivity of the ZnO material to block electron transfer during the electrocatalytic process. It is worth noting that after adding AuNPs to the ZnO surface, this issue was obviously improved. The peak current values of both oxidation and reduction exhibited a remarkable increase. In addition, although the ΔEp of the nanocomposite (0.416 V) could not be reduced to the same value as that of the bare electrode (0.365 V), it was already much lower than that of the ZnO arrays (0.467 V). This promotion is mainly derived from both the high catalytic properties and conductivity of the gold nanoparticles, which advance the electrochemical behaviours of the ZnO arrays. To further investigate the specific resistance of electron transfer, the above three electrodes were also tested by EIS scanning. Fig. 3b presents the Nyquist plots of the bare, ZnO-modified and Au–ZnO-modified ITO electrodes. The charge transfer resistance (Rct) values of these three electrodes were calculated to be 223.92, 470.06 and 310.56 Ω, respectively. This result illustrates that the introduction of AuNPs enables efficient improvement of the conductivity of ZnO, benefiting current signal amplification.

The construction of an aloe-like structure was expected to yield a high surface area, thus providing more catalytic and enzyme loading sites. To prove this assumption, the effective specific surface area of the as-prepared electrodes was studied through the following Randles-Sevcik equation (Jiang et al., 2018; Shi et al., 2014):

$$\frac{I_p}{v^{1/2}} = \left(2.69 \times 10^5\right) n^{3/2} D_0^{1/2} C_0^* A \quad (2)$$

In this equation, the parameters n, D_0 and C_0 are constant values. Hence, there is a linear relationship between the peak current and the

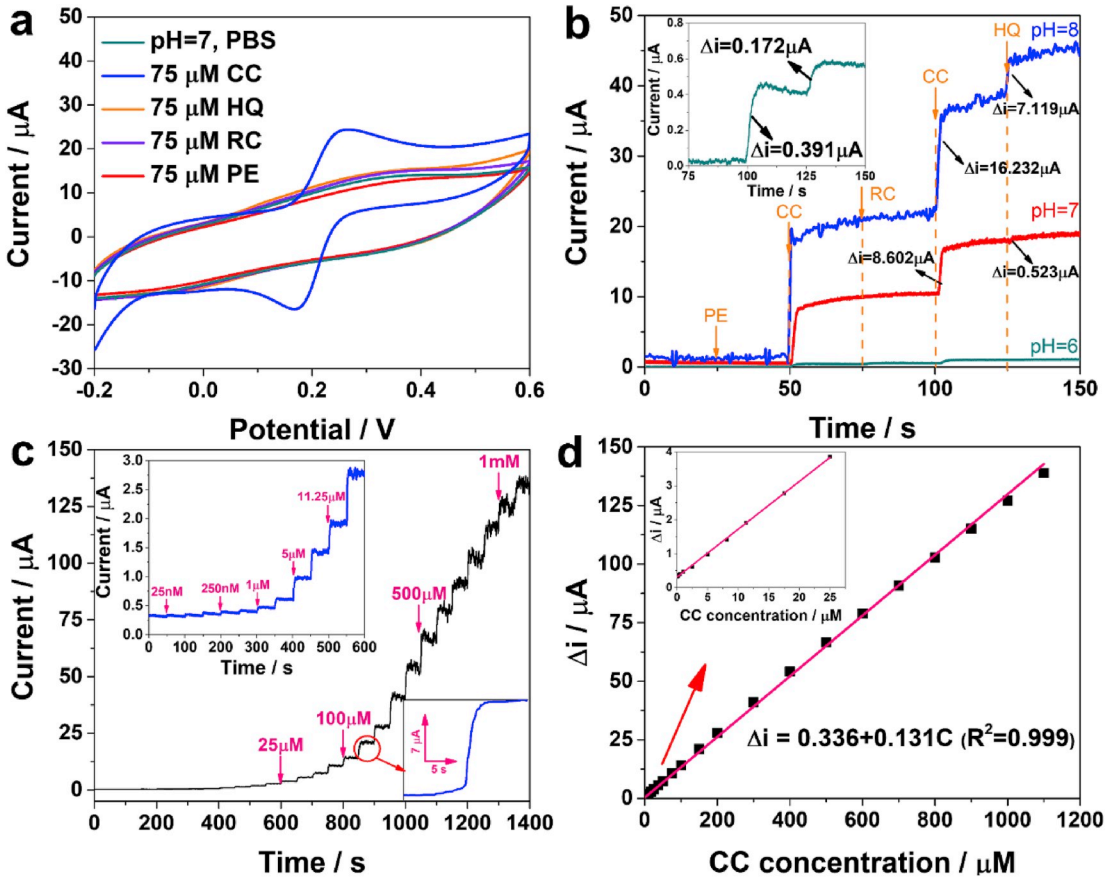

Fig. 4. (a) CV curves of the biosensor in the absence and presence of 75 μM of HQ, CC, RC and PE; (b) amperometric responses of the biosensor under different pH conditions, 75 μM of PE, CC, RC and HQ added at 50 s, 100 s, 150 s and 200 s; inset: magnification of the curve in the case of pH = 6; (c) amperometric responses of the biosensor to the repeated addition of CC every 50 s, inset: magnification of the curve from 0 to 600 s; (d) linear correlation between peak current and CC concentration; inset: magnification of the curve at low concentrations of CC.

square root of the scanning rate. Fig. 3c shows the CV performance of the bare, ZnO array-modified and Au–ZnO array-modified ITO electrodes with scan rates from 50 to 300 mV/s. According to the calibration in Fig. 3d, the effective surface area increased from 1.3 to 3.70 ± 0.08 cm^2 (Table S1) due to the double-scale structures of the aloe-like ZnO and AuNPs, which greatly enhance the electrode surface area, benefiting catalysis and enzyme loading. After the CV and EIS tests, the electrodes were rinsed with deionized water and PBS buffer. Then, laccase solution was dropped on the electrodes to prepare the biosensors.

The kinetic control mechanism of the as-prepared biosensors for CC detection was further investigated through CV characterization in the presence of 75 μM of CC. As shown in Fig. 3e, both CC redox peak currents were enhanced with increasing scanning rate. Further simulations were performed to reveal the relations between the redox peak current and scan rate (Fig. 3f). The observed linear dependences demonstrate that electrochemical CC oxidation is a diffusion-controlled process that is closely associated with the target concentration (Jiang et al., 2017; Yang et al., 2017). With increasing scan rate (10–300 mV/s), the peak potential separation (ΔEp) increased from 63 mV to 141 mV with a peak current ratio almost equal to 1, indicating that the electrode reaction corresponds to a quasi-reversible redox process (Vasilescu et al., 2016; Wen et al., 2016). In this case, the as-prepared biosensor is capable of the quantitative detection of CC.

3.3. Quantitative determination of catechol

For CC detection, laccase was selected for immobilization on the Au–ZnO array surface as the bio-recognizer. However, there are two other kinds of dihydroxybenzene, hydroquinone (HQ) and resorcinol (RS), which may produce interference during CC biosensing. Therefore, we tested the influences of phenol, HQ and RS on the electrochemical oxidation of CC. As observed in Fig. 4a, in the oxidation process, a potential below 0.4 V caused only a slight change in the current signal after the addition of 75 μM of phenol, HQ or RS. In contrast, when the same concentration of CC was added, a quite strong peak current can be created ca. 0.25 V, illustrating that the sensor is much more sensitive to CC than phenol and other dihydroxybenzenes. As reported, the environmental pH value in a detection system can greatly affect the enzyme activity and ZnO material (Chawla et al., 2012). Therefore, the chronoamperometric performance of the as-prepared biosensor in different pH environments was investigated to obtain the dynamic responses to different phenolic compounds, as shown in Fig. 4b. In solution at pH = 8, although the addition of phenol and RS did not produce any obvious current response from oxidation, the injection of 75 μM of CC and HQ produced stable current steps, showing 16.232 and 7.119 μA increases, respectively. The responses of both CC and HQ are caused by the over-oxidation behaviour of the ZnO material under the alkaline environment. OH^- ions can further oxidize Zn^{2+} to a higher valence with strong oxidizing ability. Hence, the prepared biosensor can directly catalyse CC and HQ without enzymatic assistance, serving as a nonenzymatic sensor. However, this detection selectivity is not satisfactory to determine the accurate structure of the dihydroxybenzene. In this case, we decreased the pH value to 7 to weaken the function of OH^- ions. In these conditions, the current change caused by CC was 8.602 μA, while the current response of HQ was 0.523 μA, showing only 6.1% current interference. Phenol and RS also produced little interference. Upon further reducing the pH value, the response signal generated by CC was 0.391 μA, while that generated by HQ was 0.172 μA. Compared to the

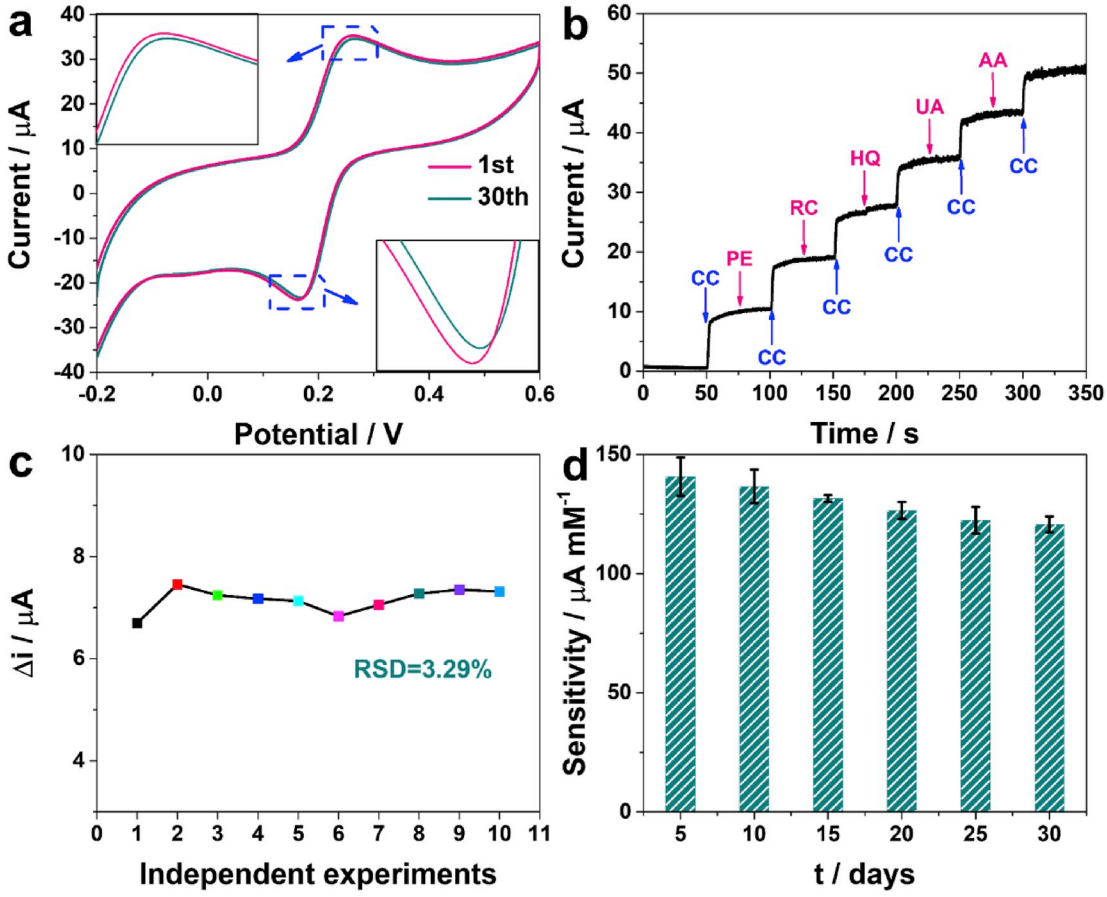

Fig. 5. (a) Stability of the biosensor after scanning in 0.05 M PBS with 75 μM of CC for 30 cycles; (b) Selectivity tests of the as-prepared CC biosensor at 0.25 V: 75 μM of CC was added every 50 s from 50 s to 300 s, and 75 μM of other interferents was added every 50 s from 75 s to 275 s. (c) Reproducibility of the biosensor in 50 μM of CC solution. (d) Stability of the sensor over one month.

case of pH = 7, this sensitivity is much lower, which may be attributed to the weaker activity of laccase under the acidic environment. Thus, an environment of pH = 7 was selected for further performance evaluation of the as-prepared biosensor.

Fig. 4c shows the online current response during the repeated introduction of CC from low to high concentrations. The biosensor can rapidly generate current steps after each addition of CC at different concentrations. It is worth mentioning that the current step value increased with increasing CC concentration. A linear relationship was achieved between the signal change (Δi) and CC concentration from 75 nM to 1.1 mM with a regression equation of $\Delta i = 0.131C_{cc} + 0.336$ ($R^2 = 0.999$) (Fig. 4d). The sensitivity of the as-prepared biosensor was calculated to be 131 μA mM^{-1} with a low detection limit of 25 nM.

Various performance metrics, including the working potential, sensitivity, linear range and detection limit, of the as-prepared biosensor were compared with those of other currently reported catechol biosensors, which are summarized in Table S2. Our prepared biosensor has the highest detection linear range, benefiting the monitoring of catechol with a wide concentration range. Moreover, among most of the nanomaterials, the as-prepared Au–ZnO arrays possess superior performance in terms of the limit of detection (LOD).

Table 1
Detection results for CC in real water samples.

Sample	Added (μM)	Found (HPLC, μM)	Found (Biosensor, μM)	RSD (%)	Recovery (%)
Tap water	0	Not detected	Not detected	–	–
	5	4.95	5.05	3.46	100.60
	10	9.94	10.03	2.13	99.78
	15	14.95	14.95	2.19	98.90
Lake water	0	Not detected	Not detected	–	–
	5	5.00	4.85	3.25	99.40
	10	9.95	10.09	2.75	101.10
	15	14.95	15.15	1.47	99.05

3.4. Stability, selectivity and reproducibility

The stability of biosensors is essential for practical applications. As shown in Fig. 5a, after 30 CV scanning cycles, both the oxidation and reduction peaks exhibited slight changes (the oxidation peak decreased by ca. 2.38%, while the reduction peak decreased by ca. 2.09%). This result showed that the Au–ZnO-based biosensor possesses excellent electrochemical redox stability in the detection process. Moreover, PE, RC, HQ, UA and AA were used as interferents to evaluate the selectivity of the as-prepared biosensor. Accordingly, 75 μM of CC and 75 μM of interferents were repeatedly injected into the detection system one by one. As shown in Fig. 5b, with the successive addition of each interfering compound, no obvious current response was produced until CC was injected again, confirming the good selectivity of the biosensor at the low working potential of 0.25 V.

Subsequently, 10 independent biosensors were tested to investigate the reproducibility. For the same detection of 50 μM of CC, the response signals of these measured electrodes were recorded, and the results are shown in Fig. 5c; a relative standard deviation (RSD) of 3.29% was obtained, indicating excellent reproducibility. In addition, this biosensor was stored at 4 °C for one month, and CC was detected every 5 days to investigate the stability of the sensor. As shown in Fig. 5d, after 30 days, the as-prepared biosensor retained approximately 85% of the

initial sensitivity, revealing its outstanding stability.

3.5. Real water sample analysis

The practical analysis ability of the as-prepared biosensor was studied by using environmental water samples, including tap water and lake water from Jinghu Lake on our campus, via standard addition methods. Prior to the test, all the water samples were filtered by using a PES microfiltration membrane (0.22 μm) to remove impurities. The detection results were compared with those of HPLC. As listed in Table 1, CC was not detected in either tap water or Jinghu Lake water by using HPLC or the biosensor. After the manual addition of CC at the same concentration, the measurement results obtained by the as-prepared biosensor were consistent with those obtained by HPLC. The RSD was in the range of 1.47%–3.46%, and the recovery was 98.90%–101.10%. These results proved that this biosensor is reliable for CC detection in real samples. In addition, especially in real water detection processes, suspended solids and heavy metal pollutants may affect the activity and stability of laccase. Therefore, water sample pretreatment is necessary to achieve reliable assay results.

4. Conclusion

In this work, we constructed an aloe-like Au–ZnO array-based catechol biosensor via a template-free method to obtain both a large specific area and excellent conductivity, greatly benefiting electrocatalysis in the laccase reaction and electron transfer for detection signal magnification. Under the optimum conditions, the as-prepared biosensor exhibited a wide linear range, an ultralow detection limit and reliable results in real water sample analysis. The anisotropic growth strategy used to construct heterogenous nanocrystals can provide inspiration for harvesting more high-performance biosensing nanomaterials with a high surface area; furthermore, this as-prepared biosensor has great potential for use in dynamic monitoring and early warning in environmental samples.

Declaration of competing interest

The authors declare that they have no known competing financial interests or personal relationships that could have appeared to influence the work reported in this paper.

CRediT authorship contribution statement

Tao Liu: Conceptualization, Methodology, Software, Investigation, Writing - original draft, Visualization. **Qiang Zhao:** Methodology, Software, Investigation, Writing - original draft. **Ying Xie:** Investigation, Data curation. **Danfeng Jiang:** Conceptualization, Methodology. **Zhenyu Chu:** Writing - review & editing, Supervision, Project administration. **Wanqin Jin:** Writing - review & editing, Supervision, Project administration, Funding acquisition.

Acknowledgements

This work was financially supported by the National Natural Science Foundation of China (No. 21706116 and 21727818), the Innovative Research Team Program by the Ministry of Education of China (No. IRT_17R54), the Top-notch Academic Programs Project of Jiangsu Higher Education Institutions (TAPP), the Priority Academic Program Development of Jiangsu Higher Education Institutions (PAPD), the Jiangsu Province Natural Science Foundation for the Youth (No. BK20180687) and the Key Project by Medical Science and Technology Development Foundation of Nanjing Department of Health (ZKX17014).

Appendix A. Supplementary data

Supplementary data to this article can be found online at https://doi.org/10.1016/j.bios.2020.112145.

References

Abbas, W., Akhtar, N., Liu, Q., Li, T., Zada, I., Yao, L., Naz, R., Zhang, W., Mazhar, M.E., Zhang, D., Ma, D., Gu, J., 2019. Sensor. Actuator. B 282, 617–625.
Ameer, Q., Adeloju, S.B., 2009. Sensor. Actuator. B 140, 5–11.
Bansod, B., Kumar, T., Thakur, R., Rana, S., Singh, I., 2017. Biosens. Bioelectron. 94, 443–455.
Bensalah, Gadri, Cañizares, P., Sáez, C., Lobato, J., Rodrigo, M.A., 2005. Environ. Sci. Technol. 39, 7234–7239.
Cardoso, A.R., Marques, A.C., Santos, L., Carvalho, A.F., Costa, F.M., Martins, R., Sales, M.G.F., Fortunato, E., 2019. Biosens. Bioelectron. 124–125, 167–175.
Chang, F.M., Brahma, S., Huang, J.H., Wu, Z.Z., Lo, K.Y., 2019. Sci. Rep. 9, 905.
Chawla, S., Rawal, R., Kumar, D., Pundir, C.S., 2012. Anal. Biochem. 430 (1), 16–23.
Cho, M., Kim, J.M., Kim, B., Yim, S., Kim, Y.J., Jung, Y.S., Oh, J., 2019. J. Mater. Chem. 7, 6045–6052.
Chu, Z., Liu, Y., Jin, W., 2017. Biosens. Bioelectron. 96, 17–25.
Fujii, S., Fukano, R., Hayami, Y., Ozawa, H., Muneyuki, E., Kitamura, N., Haga, M.-a., 2017. ACS Appl. Mater. Interfaces 9, 8413–8419.
García-Farrera, B., Velásquez-García, L.F., 2019. ACS Appl. Mater. Interfaces 11, 29167–29176.
Greene, L.E., Law, M., Tan, D.H., Montano, M., Goldberger, J., Somorjai, G., Yang, P., 2005. Nano Lett. 5, 1231–1236.
Hu, F., Liu, T., Pang, J., Chu, Z., Jin, W., 2020. Sensor. Actuator. B 306, 127587.
Jiang, D., Chu, Z., Peng, J., Jin, W., 2016. Sensor. Actuator. B 228, 679–687.
Jiang, D., Chu, Z., Peng, J., Luo, J., Mao, Y., Yang, P., Jin, W., 2018. Electrochim. Acta 270, 147–155.
Jiang, D., Li, C., Liu, T., Li, L., Chu, Z., Jin, W., Ren, X., 2017. Sensor. Actuator. B 241, 860–867.
Jiang, D., Pang, J., You, Q., Liu, T., Chu, Z., Jin, W., 2019. Biosens. Bioelectron. 124–125, 260–267.
Jiao, Y., Kilmartin, P.A., Fan, M., Quek, S.Y., 2018. Food Chem. 268, 77–85.
Kim, M., Kim, Y.K., Lim, S.K., Kim, S., In, S.-I., 2015. Appl. Catal., B 166–167, 423–431.
Lee, Y.W., Lim, M.A., Kang, S.W., Park, I., Han, S.W., 2011. Chem. Commun. 47, 6299–6301.
Liu, T., Chu, Z., Jin, W., 2019. J. Mater. Chem. B 7, 3620–3632.
Moldoveanu, S.C., Kiser, M., 2007. J. Chromatogr. A 1141, 90–97.
Palanisamy, S., Ramaraj, S.K., Chen, S.M., Yang, T.C.K., Yi-Fan, P., Chen, T.W., Velusamy, V., Selvam, S., 2017. Sci. Rep. 7, 41214.
Parize, R., Garnier, J., Chaix-Pluchery, O., Verrier, C., Appert, E., Consonni, V., 2016. J. Phys. Chem. C 120, 5242–5250.
Samphao, A., Butmee, P., Saejueng, P., Pukahuta, C., Švorc, Ľ., Kalcher, K., 2018. J. Electroanal. Chem. 816, 179–188.
Sani, N.D.M., Heng, L.Y., Marugan, R.S.P.M., Rajab, N.F., 2018. Food Chem. 269, 503–510.
Shahamirifard, S.A., Ghaedi, M., 2019. Biosens. Bioelectron. 141, 111474.
Shetti, N.P., Bukkitgar, S.D., Reddy, K.R., Reddy, C.V., Aminabhavi, T.M., 2019. Biosens. Bioelectron. 141, 111417.
Shi, L., Chu, Z., Liu, Y., Jin, W., Xu, N., 2014. Adv. Funct. Mater. 24, 7032–7041.
Shi, L., Wang, Y., Ding, S., Chu, Z., Yin, Y., Jiang, D., Luo, J., Jin, W., 2017. Biosens. Bioelectron. 89, 871–879.
Usha, S.P., Gupta, B.D., 2018. Biosens. Bioelectron. 101, 135–145.
Vasilescu, I., Eremia, S.A.V., Kusko, M., Radoi, A., Vasile, E., Radu, G.L., 2016. Biosens. Bioelectron. 75, 232–237.
Wang, H., Li, H., Huang, Y., Xiong, M., Wang, F., Li, C., 2019. Biosens. Bioelectron. 142, 111531.
Wang, Z., Li, S., Lv, Q., 2007. Sensor. Actuator. B 127, 420–425.
Wen, Y., Wen, W., Zhang, X., Wang, S., 2016. Biosens. Bioelectron. 79, 894–900.
Yang, P., Peng, J., Chu, Z., Jiang, D., Jin, W., 2017. Biosens. Bioelectron. 92, 709–717.
Ying, Y., Pourrahimi, A.M., Manzanares-Palenzuela, C.L., Novotny, F., Sofer, Z., Pumera, M., 2019. Small, p. 1902944.
You, Q., Liu, T., Pang, J., Jiang, D., Chu, Z., Jin, W., 2019. Sensor. Actuator. B 296, 126617.
Yue, H.Y., Song, S.S., Guo, X.R., Huang, S., Gao, X., Wang, Z., Wang, W.Q., Zhang, H.J., Wu, P.F., 2019. J. Electroanal. Chem. 838, 142–147.
Zhao, M., Li, Z., Han, Z., Wang, K., Zhou, Y., Huang, J., Ye, Z., 2013. Biosens. Bioelectron. 49, 318–322.